Proper orthogonal decomposition and low-dimensional models for driven cavity flows

Cazemier, W; Verstappen, R.W.C.P.; Veldman, A.E.P.

Published in:
Physics of Fluids

DOI:
10.1063/1.869686

Proper orthogonal decomposition and low-dimensional models for driven cavity flows

W. Cazemier,[a] R. W. C. P. Verstappen, and A. E. P. Veldman
Department of Mathematics, University of Groningen, P.O. Box 800, 9700 AV Groningen, The Netherlands

(Received 1 April 1997; accepted 3 March 1998)

A proper orthogonal decomposition (POD) of the flow in a square lid-driven cavity at $Re=22{,}000$ is computed to educe the coherent structures in this flow and to construct a low-dimensional model for driven cavity flows. Among all linear decompositions, the POD is the most efficient in the sense that it captures the largest possible amount of kinetic energy (for any given number of modes). The first 80 POD modes of the driven cavity flow are computed from 700 snapshots that are taken from a direct numerical simulation (DNS). The first 80 spatial POD modes capture (on average) 95% of the fluctuating kinetic energy. From the snapshots a motion picture of the coherent structures is made by projecting the Navier–Stokes equation on a space spanned by the first 80 spatial POD modes. We have evaluated how well the dynamics of this 80-dimensional model mimics the dynamics given by the Navier–Stokes equations. The results can be summarized as follows. A closure model is needed to integrate the 80-dimensional system at $Re=22{,}000$ over long times. With a simple closure the energy spectrum of the DNS is recovered. A linear stability analysis shows that the first (Hopf) bifurcation of the 80-dimensional dynamical system takes place at $Re=7{,}819$. This number lies about 0.7% above the critical Reynolds number given in Poliashenko and Aidun [J. Comput. Phys. **121**, 246 (1995)] and differs by about 2% from the first instability found with DNS. In addition to that, the unstable eigenvector displays the correct mechanism: a centrifugal instability of the primary eddy, however, the frequency of the periodic solution after the first bifurcation differs from that of the DNS. The stability of periodic solutions of the 80-dimensional system is analyzed by means of Floquet multipliers. For $Re=11{,}188-11{,}500$ the ratio of the two periods of the stable 2-periodic solution of the 80-dimensional system is approximately the same as the ratio of the two periods of the 2-periodic solution of the DNS at $Re=11{,}000$. For slightly higher Reynolds numbers both solutions lose one period. The periodic solutions of the dynamical system at $Re=11{,}800$ and the DNS at $Re=12{,}000$ have approximately the same period and have qualitatively the same behavior. © *1998 American Institute of Physics.* [S1070-6631(98)03006-2]

I. INTRODUCTION

Coherent structures catch the eye in virtually every visualization of a turbulent flow. Lumley[1] was the first who used proper orthogonal decomposition (POD) to identify the coherent structures in a flow. At that time, the basic technique was already known among statisticians; they called it Karhunen–Loève expansion.[2]

A velocity field, say $u(x,t)$, is usually decomposed linearly. Among all linear decompositions, the proper orthogonal decomposition $\Sigma_i a_i(t)\sigma_i(x)$ is the most efficient in the sense that the POD captures the largest possible amount of kinetic energy (for any given number of modes). In 1991, Aubry[3] uncovered a till then hidden beauty of the POD: it yields an optimal, orthogonal, spatial basis as well as an optimal, orthogonal, temporal basis. The projection of $u(x,t)$ on the σ_i's/a_i's converges faster (in quadratic means) than the projection on any other spatial/temporal basis, with the same number of elements.

We will use the space–time symmetry to compute the POD of a flow in a square, lid-driven cavity at a Reynolds number of $Re=22{,}000$. The input data for the POD consists of flow fields that have been computed by a direct numerical simulation (DNS). Results and details of the DNS are given in Section II. A sketch of the basic idea of POD, the discretization, the computational method, and the results for the driven cavity can be found in Section III. Further results (also in three spatial dimensions) can be found in Ref. 4.

Having a way to educe coherent structures in a driven cavity flow, the next question that can be posed, reads as follows: how do these structures move, interact, survive, during the early stages of transition to turbulence. Nowadays, the idea has taken form that the dynamics is low-dimensional (see e.g., Témam[5]). This implies that the transitional behavior of the flow may be described in terms of a few ordinary differential equations. In Section IV we will utilize the optimality of the spatial basis $\{\sigma_i\}$ to derive low-dimensional models for driven cavity flows.

Low-dimensional models have been considered for a number of flows; we mention the examples that can be found in Refs. 6–10. For further examples the reader is referred to

[a]Present address: The Netherlands Organization For Applied Scientific Research (TNO), Section Computational Mechanics, P.O. Box 49, Delft, The Netherlands.

the overview paper by Berkooz, Holmes, and Lumley[11] or to their recent book.[12] In all these references, low-dimensional dynamical models are constructed by projecting the Navier–Stokes equations on a space spanned by a small number of σ_i's. Aubry *et al.*[6] were among the pioneers. They considered the motion of coherent structures in the wall region of a turbulent boundary layer. Deane *et al.* applied the method to grooved channels and circular cylinders in Ref. 7 and to the wake of a flow past an airfoil in Ref. 8; Glauser *et al.*[9] applied it to an axisymmetric jet mixing layer; Rempfer[10] considered a flate-plate boundary layer.

From a theoretical point of view, it is not clear how well POD modes, and the low-dimensional models based on them, perform at Reynolds numbers different from the one at which they were constructed. By construction, POD modes form a complete set of basis functions (satisfying the boundary conditions and the incompressibility constraint) for all Reynolds numbers, but this basis set is optimal for one Reynolds number only. So far, a few—encouraging—practical experiences concerning the robustness of POD modes have been reported. In all these cases, some kind of scaling (of the mean flow, or of all modes) is performed; see also Ref. 13. For near-wall flows (like in Ref. 6) the scaling is obvious: everything can be expressed in terms of wall variables, and thus a universal scaling can be brought into the basis functions. Liu *et al.*[14] have shown that, also in the outer layer of a wall-bounded turbulent flow, the one-dimensional POD is (almost) independent of the Reynolds number when it is scaled by the wall friction velocity and the outer length scale.

For complex flows, appropriate scalings of the underlying physics are often lacking. Deane *et al.*[7] have shown that it is possible to obtain a fairly accurate description of some complex flows by means of a low-dimensional system that is based on a POD at a particular value of the Reynolds number. They considered two complex flows: a flow in a grooved channel and a flow past a circular cylinder. In both cases they modified the mean flow to tackle a range of Reynolds numbers. In the wake of the cylinder, the low-dimensional model of Deane *et al.* is only valid for a small neighborhood of the Reynolds number for which the decomposition was computed. In the case of the grooved channel, they observed a larger range of Reynolds numbers for which their model is valid. Noack and Eckelmann[15] have studied low-dimensional Galerkin methods for the cylinder wake, too (with ''mathematical'' modes instead of POD modes). They concluded that the success of their method is insensitive to a reasonal choice of the basic mode, but depends crucially on the choice of a weight parameter that they introduced in the inner product.

In this paper, we apply POD to a 2D flow in a square, lid-driven cavity at Reynolds number $Re=22{,}000$ and use this empirical basis to model driven cavity flows for a range of Reynolds numbers. Here, we take one set of basis functions, without scaling them, to investigate the range of Reynolds numbers for which this approach yields a valid model. In a future sequel to this research, the observed shortcomings of the model may be overcome by scaling the basis functions in a proper way, or by adding basis functions of other Reynolds numbers, or by modifying the basis iteratively (as in Ref. 13, for instance). The ability of the model to mimic the DNS for Reynolds numbers lower than 22,000 is studied numerically by means of a bifurcation analysis. To that end, the first 80 σ_i's of the flow in a lid-driven cavity at $Re=22{,}000$ have been computed. Projecting the Navier–Stokes equation on them yields a 80-dimensional model. The basis is optimal for $Re=22{,}000$, but what about the model: is it able to mimic the transition behavior of the flow in a lid-driven cavity? This question is addressed in Section V. DNS results are available for comparison (see Section II C).

II. DIRECT NUMERICAL SIMULATION

The input data for the POD consists of flow fields that are computed by a direct numerical simulation (DNS) of a flow in a two-dimensional driven cavity at Reynolds number $Re=22{,}000$. The simulation method is outlined in Section II A. Results are briefly presented in Section II B. Direct numerical simulations have also been performed for Reynolds numbers in the range $Re=8{,}000-16{,}000$ to obtain reference data for the transition analysis of low-dimensional models for driven cavity flows. DNS results for $Re=8{,}000-16{,}000$ can be found in Section II C.

A. Simulation method

We consider the flow in a square, lid-driven cavity. All lengths are made dimensionless by taking the height of the cavity as a unit length; velocities are made dimensionless with the help of the speed at which the lid is driven. No-slip conditions are imposed at all walls. For the computation of the POD data, the velocity field is discretized on a 333^2 staggered grid. The incompressible Navier–Stokes equations are solved using a second-order accurate, finite-volume method, where the spectral properties of the convective and diffusive operators are preserved, i.e., convection $\leftrightarrow$ skew-symmetric; diffusion $\leftrightarrow$ symmetric positive-definite; see Ref. 16. The pressure gradient and the incompressibility constraint are integrated implicitly in time (using backward Euler); the convective and diffusive fluxes are treated explicitly (second-order Adams–Bashforth). The pressure is solved using the conjugate gradient method with a modified incomplete Choleski preconditioner.[17,18]

The first few bifurcations of the low-dimensional models will be compared to the results of DNS in Section V. For these direct numerical simulations a fourth-order spatial discretization method is used that also preserves the spectral properties of the convection and diffusion. A detailed discussion of the spatial discretizations, including a comparison with other schemes, can be found in Refs. 19 and 20.

B. Data for the POD: Results at *Re*=22,000

The database of flow fields for the POD originates from a direct numerical simulation of a two-dimensional flow in a lid-driven cavity at $Re=22{,}000$. Figure 1 shows the vorticity of the mean flow in the cavity. It takes roughly five time units for the primary eddy in the core of the cavity to turn around. We call this period a large-eddy turnover-time. At $Re=22{,}000$ vortical structures move seemingly chaotically around in the cavity along trajectories that stay relatively

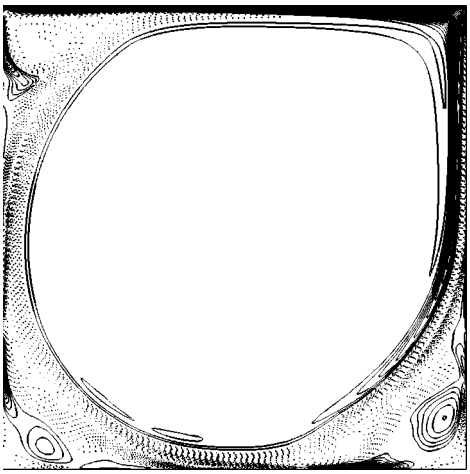

FIG. 1. The vorticity of the mean flow as obtained from a DNS of a lid-driven cavity flow at $Re=22{,}000$. In this figure, and in all following figures of driven cavities, the orientation of the cavity is such that the upper lid is driven from the left to the right. Solid lines indicate a clockwise rotation; dashed lines indicate counter-clockwise rotation.

close to the walls of the cavity. In Ref. 21 we have estimated the Kolmogorov entropy K from the correlation integral (in the manner that is outlined in Refs. 22 and 23). A chaotic, deterministic system is characterized by $0<K<\infty$, an ordered system by $K=0$, and a random system by $K=\infty$. We found $K\approx 3$. Thus, the dynamical behavior is chaotic.

The DNS of the driven cavity flow at $Re=22{,}000$ consists of two separate simulations that start from different initial conditions. Both start from earlier computed velocity fields that are statistically in equilibrium. The first run covers 500 time units; the second one lasts six times longer. So, in total, 700 large-eddy turnover-times have been computed. The integral of the kinetic energy over the spatial domain as obtained from both runs is shown in Fig. 2(a). The first 500 time units correspond to the first run; the rest (from 500 to 3500) belongs to the second run. The integral of the fluctuating kinetic energy of both runs is shown in Fig. 2(b). It may be noted that the level of the fluctuating energy is approximately 1.2% of the total energy. Two sharp peaks in the fluctuating kinetic energy and two (corresponding) deep valleys in the kinetic energy stand out. These catastrophes occur after $\pm$ 2300 time units and after $\pm$ 3400 time units. At these two times an eddy penetrates the core region of the cavity. Figure 3 catches such an intruder in the act. This eddy originates in the shear-layer along the right-hand wall of the cavity. From there it is advected along the walls (in the clockwise direction) to the upper-wall. This part of the journey is ordinary: many eddies make it up to here. Yet, they are all flattened up against the upper-wall of the cavity and vanish soon after that. The eddy that is shown in Fig. 3 is not squeezed flat when it arrives at the lid, but it is ejected into the core region and crosses the cavity. Its journey ends near the lower left-hand corner, where it vanishes. As far as we know, this phenomenon has not been observed before in a square, lid-driven cavity. In a cylindrical vessel with a rotating cover, however, a similar phenomenon has been observed, both in an experimental and in a numerical study; see

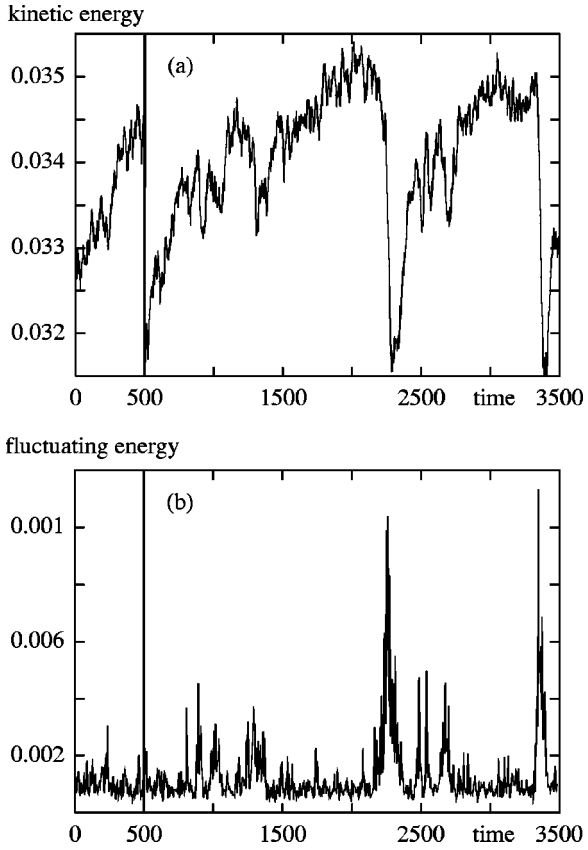

FIG. 2. Time-series of the kinetic energy (a) and of the fluctuating kinetic energy (b) in a square lid-driven cavity at $Re=22{,}000$. Both quantities are integrated over the spatial domain.

Ref. 24. The visualization of the flow in the vessel shows also a large eddy that crosses the vessel.

C. (Quasi-)periodic driven cavity flows

In many papers on driven cavity flows steady states have been reported at $Re=10{,}000$. Often flow computations in a two-dimensional (2D) lid-driven cavity by Ghia *et al.*[25] are taken as a reference for steady state solutions of the Navier–

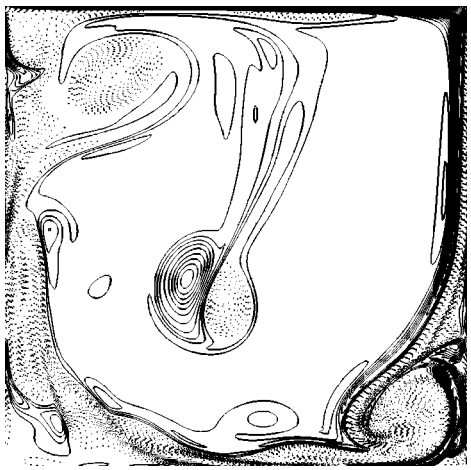

FIG. 3. A rarity which occurred only twice during 700 large-eddy turnover-times: an eddy has penetrated the core region of the cavity. This figure shows the vorticity; $Re=22{,}000$.

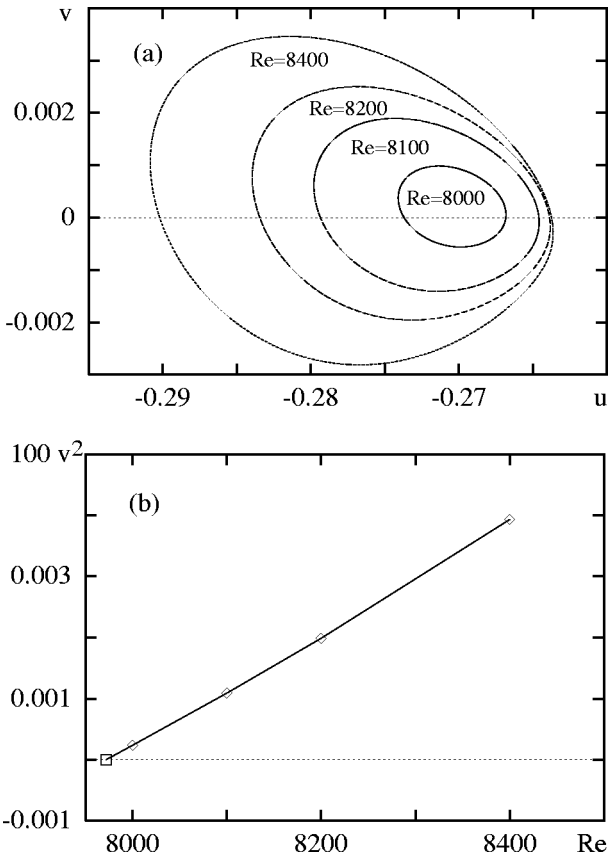

FIG. 4. Phase plot of the horizontal velocity u versus the vertical velocity v in a point $(x,y)=(0.5, 0.02)$ (a) and a plot of the square of $v(0.5, 0.02)$ versus the Reynolds number (b). The critical Reynolds number is extrapolated from the latter.

Stokes equations up to and including $Re=10{,}000$. Yet, the flow goes unstable, becomes periodic in time, bifurcates once more, and becomes two-periodic for $Re<10{,}000$. The first bifurcation, from steady to periodic, has been investigated by Poliashenko and Aidun.[26] They showed that the steady state in a driven cavity becomes unstable at $Re=7{,}763\pm 2\%$.

To put the critical Reynolds number beyond doubt, we have performed a fourth-order accurate DNS at $Re=7{,}800$. However, we could not observe a periodic solution at this Reynolds number. The lowest Reynolds number at which the DNS yielded a clearly visible periodic solution was $Re=8{,}000$. It is known for the Hopf bifurcation (see, for instance, Ref. 27) that the amplitude of the solution grows (in first-order approximation) with the square-root of the bifurcation parameter. In our case, this means that the square of a velocity component should be proportional to the difference of the Reynolds number Re and the critical Reynolds number after the bifurcation has taken place. To verify this, we have performed direct numerical simulations at the Reynolds numbers 8,100, 8,200, and 8,400. A phase plot of a horizontal velocity u against a vertical velocity v at a point near the bottom of the cavity is shown in Fig. 4. The plot of the square of the v versus the Reynolds number is approximately a straight line. This line can be extrapolated to where it crosses the zero axis to approximate the bifurcation point,

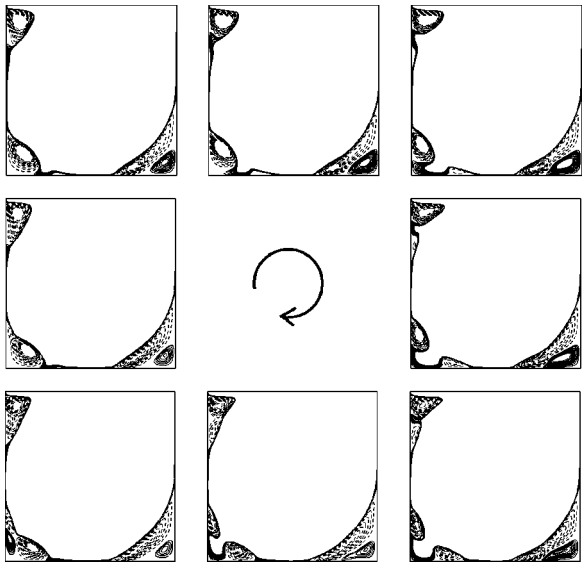

FIG. 5. Streaklines of one period of the periodic solution of the DNS at $Re=12{,}000$. Solid lines indicate a clockwise rotation, and dashed lines indicate counter-clockwise rotation.

which gives a critical value of approximately $Re=7{,}972$. This number lies about 2.6% above the critical Reynolds number of Poliashenko and Aidun.[26] In addition to that, the frequency of the periodic solution in Ref. 26 $(2.86\pm 1\%)$ agrees well with the frequency that rolled out of the DNS (2.85).

Recently, the quasi-periodic nature of the flow at Re $=10{,}000$ has been mentioned in Ref. 28. To demonstrate that the flow is two-periodic at $Re=10{,}000$, we have performed three direct numerical simulations at $Re=10{,}000$. One with a second-order accurate finite-volume method (on a 333^2 grid) and two with the fourth-order method using a 250^2 grid and a 500^2 stretched grid, respectively. All three simulations gave a quasi-periodic solution with two fundamental frequencies: $f_1\approx 2.7$ and $f_2\approx 1.7$. The same two fundamental frequencies are also present in the time-series obtained from a DNS of the flow in a driven cavity at $Re=11{,}000$.

By playing with the initial conditions, we have found two different periodic solutions at $Re=12{,}000$. The frequencies are subharmonics of those at $Re=11{,}000$, namely, $2f_1-f_2$ and f_1+f_2. Figure 5 shows the creation, motion, and merging of eddies near three corners of the cavity for the periodic solution with the frequency $2f_1-f_2$. A return from a quasi-periodic state to a periodic state has been observed experimentally in a cylindrical lid-driven cavity too: Sørensen *et al.*[29] noted that a two-periodic flow in a cylindrical cavity loses one period when the Reynolds number is increased.

We have computed periodic solutions with a frequency of approximately $2f_1-f_2$ for the Reynolds numbers 14,000, 15,000, and 16,000. Periodic solutions with the frequency f_1+f_2 came out the DNS at $Re=12{,}000$ and $Re=13{,}000$.

III. PROPER ORTHOGONAL DECOMPOSITION

To make this paper self-contained, we will sketch the main lines of Proper Orthogonal Decomposition (POD) in

Section III A. Hereby, the space–time symmetry is emphasized (like in Ref. 3) since this property leaves us the option between solving (discrete) eigenproblems for the spatial basis $\{\sigma_i\}$ or for the temporal basis $\{a_i\}$. The latter option requires much less computational work (see Section III B) and is thus preferred. The temporal discretization is done by snapping the fluctuating flow in the driven cavity every time the primary eddy has turned over. The use of those snapshots has been proposed by Sirovich.[30] Results of the POD of the flow in a driven cavity at $Re=22{,}000$ are presented in Section III C.

A. Continuous formulation

We consider a velocity field $u(x,t)$, where the spatial variable x and the time t are elements of Ω and T, respectively. The basic idea of POD consists of finding the ''best'' approximation of $u(x,t)$ in terms of N spatial components (the POD modes) $\sigma_i(x)$, $i=1,..,N$ and N temporal functions (the time traces of modal energies) $a_i(t)$, $i=1,..,N$. The spatial and temporal components are solved from

$$\min \int_{\Omega T} \int \left(u(x,t) - \sum_{i=1}^{N} a_i(t)\sigma_i(x) \right)^2 dt dx. \tag{3.1}$$

Arbitrary variations of the unknowns $\sigma_i(x)$ and $a_i(t)$ yield

$$\left\langle \left(u - \sum_j a_j \sigma_j \right) a_i \right\rangle_T = 0 = \left\langle \left(u - \sum_j a_j \sigma_j \right) \sigma_i \right\rangle_\Omega, \tag{3.2}$$

where an integration over Ω is denoted by $\langle \cdot \rangle_\Omega$, and an integration over T by $\langle \cdot \rangle_T$. To solve these Euler–Lagrange equations, we assume that $\langle \sigma_i \sigma_j \rangle_\Omega = 0 = \langle a_i a_j \rangle_T$ for $i \neq j$, and verify this afterwards. Under this assumption, Eq. (3.2) can be written as $\sigma_i = \langle u a_i \rangle_T / \langle a_i^2 \rangle_T$ and $a_i = \langle u \sigma_i \rangle_\Omega / \langle \sigma_i^2 \rangle_\Omega$. Substituting the latter (former) expression into the former (latter) shows that the spatial (temporal) components are the eigenfunctions of the integral operator with the temporal (spatial) auto-correlation as a kernel:

$$\lambda_i \sigma_i(x) = \int_\Omega \langle u(x,t)u(x',t) \rangle_T \sigma_i(x') dx', \tag{3.3}$$

$$\mu_i a_i(t) = \int_T \langle u(x,t)u(x,t') \rangle_\Omega a_i(t') dt'. \tag{3.4}$$

These eigenvalue problems are Fredholm integral equations of the second type, with positive definite Hermitian kernels. The properties of these equations are given by the Hilbert–Schmidt theorem (see, for example, Ref. 31). This theorem states that the eigenfunctions are orthogonal. Hence, they are solutions of Eq. (3.1). In addition, Hilbert–Schmidt states that the eigenvalues λ_i and μ_i are real and positive, and that the flow field $u(x,t)$ can be (fully) reconstructed from the eigenfunctions if $N=\infty$.

Eigenfunctions need to be normalized. It is common practice to normalize the spatial eigenfunctions: $\langle \sigma_i^2 \rangle_\Omega = 1$. The norm of a_i is then given by $\langle a_i^2 \rangle_T = \lambda_i$. An eigenvalue λ_i can thus be interpreted as the average amount of energy in the direction of the corresponding POD mode. To obtain the ''best'' approximation of $u(x,t)$ in terms of N eigenfunctions, the eigenvalues are ordered in increasing magnitude: λ_1 is the largest eigenvalue, λ_2 is the second largest, and so on (till λ_N).

It may be noted that a POD can be computed of the entire velocity field $u(x,t)$ or of its fluctuating part $u'(x,t) = u(x,t) - \langle u(x,t) \rangle_T$. Often, a POD is based on the fluctuating field. The POD of the entire velocity field and the POD of the fluctuating field are essentially the same when $\langle \langle u(x,t)u(x,t') \rangle_\Omega \rangle_T$ is constant. Indeed, then $a_i =$ constant is an eigenfunction [i.e., a solution of (3.4)] and the corresponding mode $\sigma_i = \langle u a_i \rangle_T / \langle a_i^2 \rangle_T$ is a constant times $\langle u \rangle_T$.

B. Discretization and computational method

A DNS yields velocities $u^{n,m}$ at grid points x^n and at time levels t^m. Consequently, the POD technique is to be discretized. Then, the spatial and temporal integrations in (3.1) become summations over n and m. We denote the resulting summations by $\langle \cdot \rangle_n$ and $\langle \cdot \rangle_m$, respectively. To discretize a temporal (or spatial) integral, we subdivide the interval of integration into subintervals and in each subinterval approximate the integrand by a constant, the value of the integrand at the time level (grid point) nearest to the midpoint of the subinterval. Thus, at a grid point x^n, the integral of u over an interval in time is approximated by

$$\langle u \rangle_m = \sum_{m=1}^{M} u^{n,m} (dt_m + dt_{m+1})/2, \tag{3.5}$$

where the time spacing in between two successive snapshots of the velocity field is given by $dt_m = t^m - t^{m-1}$. In the sequel, we will restrict ourselves to uniform spacings in time: $dt_m = dt =$ constant. The grid used for a spatial integration is identical to that of the DNS. After discretization, the eigenproblems (3.3) and (3.4) become eigenvalue problems for matrices. The dimension of the matrix in the discrete representation of (3.3) is equal to the number of grid points; the dimension of the matrix of the discretization of (3.4) is equal to the number of time levels.

Fortunately, we do not have to solve both eigenproblems. Indeed, we can solve the discrete spatial (temporal) eigenvalue problem and compute the discrete temporal (spatial) eigenfunctions directly from the discrete Euler–Lagrange equation that results from $\delta\sigma_i = 0$ ($\delta a_i = 0$). In our case, the option between parentheses is the cheapest; the alternative leads to an eigenvalue problem of the order of 10^5 (the number of grid points). So, we solve the discrete time-traces of model energies $a_i = (a_i^1, \ldots, a_i^M)$ at time $t^1, \ldots, t^M$ from the eigenvalue problem

$$\underline{\tilde{\mu}}_i \underline{a}_i = \underline{R} \underline{a}_i, \quad \text{where } R_{m,m'} = \langle u^{n,m} u^{n,m'} \rangle_n dt \tag{3.6}$$

[i.e., from the discretization of (3.4)] and compute the i-th POD modes at grid point x^n from the discrete Euler–Lagrange equation,

$$\sigma_i^n = \frac{\langle u^{n,m} a_i^m \rangle_m}{\langle a_i^m a_i^m \rangle_m}, \tag{3.7}$$

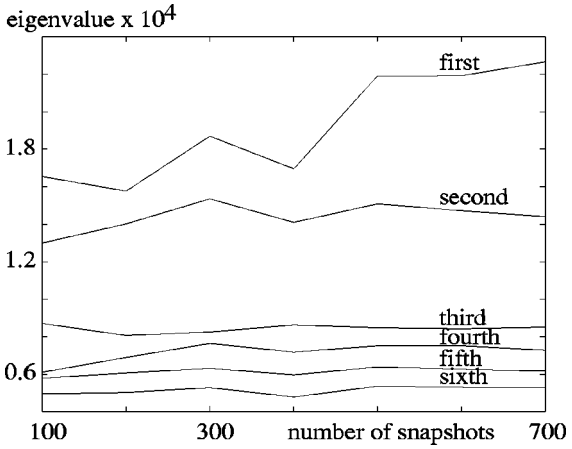

FIG. 6. Convergence of the first six eigenvalues as function of the number of snapshots.

TABLE I. Some characteristic eigenvalues of the POD of the 2D driven cavity at $Re=22{,}000$. The right column shows the relative energy of the projection of the fluctuating velocity field on the first i eigenfunctions (in the time average).

i	$\tilde{\lambda}_i$	% energy
1	2.30765×10^{-4}	18.14
2	1.44456×10^{-4}	29.50
3	8.56222×10^{-5}	36.23
4	7.28991×10^{-5}	41.96
5	6.17286×10^{-5}	46.81
6	5.35092×10^{-5}	51.02
7	4.45789×10^{-5}	54.53
8	3.81593×10^{-5}	57.53
9	3.06833×10^{-5}	59.94
10	2.94565×10^{-5}	62.25
20	1.28227×10^{-5}	77.64
40	4.12892×10^{-6}	88.69
80	1.15345×10^{-6}	95.43

where the eigenvectors of the correlation matrix R are normalized such that $\langle \sigma_i^n \sigma_i^n \rangle_n = 1$.

The time dt in between two successive snapshots should be large enough for the snapshots to be (almost) uncorrelated. This requirement is identical to the one put forth by Sirovich.[30] In contrast to Ref. 30, it is here not strictly necessary to have uncorrelated states of the flow, but it is advantageous from a numerical point of view, because it leads to a better posed eigenproblem.

As usual, we will compute the POD of the fluctuating velocity field. *A priori*, we do not know how many snapshots M should be taken for the eigenvalues $\tilde{\mu}_i$ in (3.6) and $\tilde{\lambda}_i = \langle a_i^m a_i^m \rangle_m$ to approximate the eigenvalues μ_i in (3.4) and λ_i in (3.3) accurately. In fact, we have no alternative but to try different values of $M \geqslant N$ and thus to estimate the speed of convergence of $\tilde{\mu}_i$ and $\tilde{\lambda}_i$ as a function of M.

C. POD of driven cavity flow

We have approximated the POD modes using snapshots of the fluctuating velocity from a two-dimensional DNS of a driven cavity flow at $Re=22{,}000$. Successive snapshots are (almost) uncorrelated if they are separated by five time units, i.e., by one large-eddy turnover-time. Their correlation is then less than 0.1. To reduce the correlation further, the snapshots need to be separated by many more turnover-times: the correlation decays (almost) monotone; a separation of ten large-eddy turnover-times yields a correlation of about 0.05.

The flow is snapped every time when the primary eddy has turned over. Thus, $M=700$ uncorrelated snapshots are available. This number of snapshots is chosen as large as reasonably possible for an accurate computation of the POD eigenfunctions. The first 80 eigenfunctions have been computed. The convergence of the eigenvalues $\tilde{\lambda}_i$ for $i=1,\ldots,6$ as a function of the number of snapshots is shown in Fig. 6. The eigenvalues $\tilde{\lambda}_i$ are not fully converged for $M=700$. Unfortunately, the computation of much larger values of M, 7000, for example, is rather expensive. In fact, 700 large-eddy turnover-times is already a long period for a DNS. Partly, the slow convergence of $\tilde{\lambda}_i$ towards λ_i may be explained by eddies that enter the core region at extreme long time-intervals (Figure 3 shows an example). This phenomenon is certainly not represented well in the data. For that it occurs too infrequently: of the 700 snapshots only a few will contain information about this rare phenomenon. It may be observed that the eigenvalues with the higher indices seem to have converged somewhat better than the first two. This supports the idea that long-wave phenomena have not fully converged yet.

The eigenfunctions that have been computed from the snapshots may not be as optimal as the exact eigenfunctions are. The captured energy, however, converges rapidly, and that is the crux of the matter. The first few eigenfunctions contain most of the fluctuating kinetic energy. To illustrate this, some eigenvalues are listed in Table I. Note that the average amount of turbulent kinetic energy in the ''direction'' of σ_i^n is equal to the corresponding eigenvalue $\tilde{\lambda}_i$. The first eigenfunction contains (on average) 18% of the fluctuating kinetic energy. The first 20, 40, and 80 eigenfunctions contain (on average) 77%, 88%, and 95% of the total fluctuating energy, respectively. The number of eigenfunctions that is required to capture 95% of the energy (here: 80) is an indication of the complexity of the signal $u'(x,t)$. Under some ergodicity assumptions, this number is also a measure for the complexity of the underlying attractor (which then is represented by the σ_i's).

POD eigenfunctions are optimal in the sense that every other set of the same number of modes contains less energy (in a time average) than POD eigenfunctions do. To illustrate this we have compared the (approximate) POD eigenfunctions with Fourier-modes. For that purpose a Fourier-transform of the discrete fluctuating velocity has been computed at all grid points. The resulting 333^2 Fourier-coefficients are ordered by magnitude: the largest first. This gives the optimal ordering for the Fourier-modes. Yet, even in this order, the energy contained by the first N Fourier-modes is significantly smaller than the energy contained by $\sigma_1^n, \ldots, \sigma_N^n$; see Fig. 7. Thus, as expected, the (approximate)

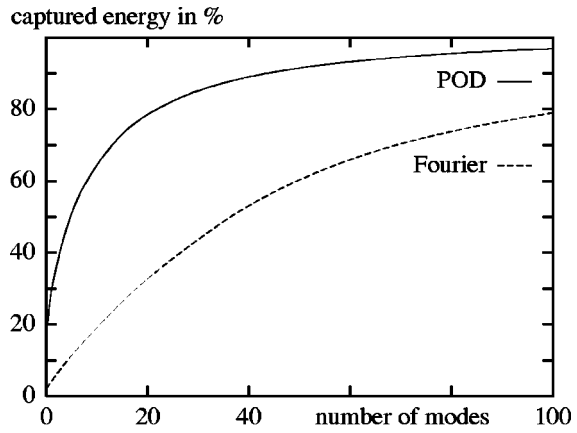

FIG. 7. Comparison of POD and Fourier-modes: captured fluctuating energy.

POD modes converge much faster than Fourier-modes.

The first six σ_i^n's are shown in Fig. 8. The eigenfunctions of the spatial auto-correlation $\langle u(x,t)u(x',t)\rangle_T$ are Fourier-modes if the auto-correlation is invariant under translations, i.e., depends only on the difference between x and x'. Fourier-modes can be grouped in pairs, e.g., $\sin(x)$ and $\cos(x)$ form a pair; they differ by a shift over one quarter of their period, and the rule $a\cos(x)+b\sin(x)=(a^2+b^2)^{1/2}\cos(x\pm\delta)$ with $\tan(\delta)=\mp a/b$, provides the construction for a complete description of the evolution of a ''cosine-wave.'' Figure 8 suggests that the leading POD modes in a lid-driven cavity can be grouped in pairs too. The first two (σ_1^n and σ_2^n) form a pair; σ_2^n is approximately a quarter out of phase compared to σ_1^n. With the first two eigenfunctions only, a motion of an eddy in the lower right corner of the cavity can be represented. Moreover, σ_3^n and σ_4^n form a pair. With them an eddy moving in the lower part of the cavity can be represented. Rempfer and Fasel[10] found that the leading POD-modes in a flat plate transitional boundary layer occur approximately in pairs, too. The fact that the leading POD-modes (in a driven cavity as well as in a transitional boundary layer) occur in pairs is likely a result of an approximate invariance of the auto-correlation. In general, however, coherent structures do not appear as pairs of POD-modes (in Ref. 6 an example can be found where individual coherent structures can not be formed by a pair of POD-modes).

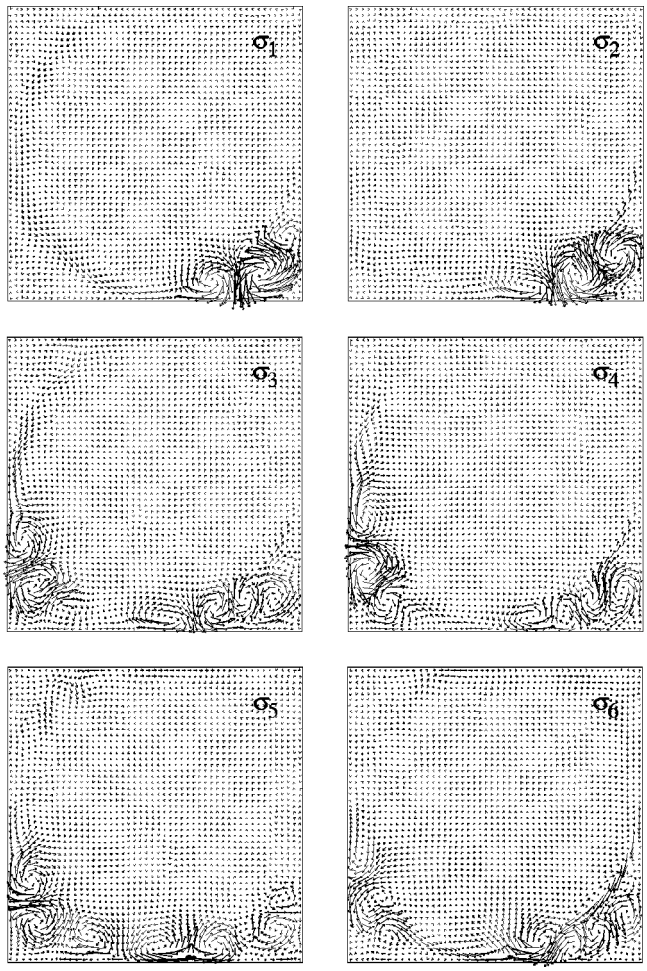

FIG. 8. Vector plots of the eigenfunctions $\sigma_1-\sigma_6$. The numbering goes in reading order: the upper left picture shows σ_1; the lower right one depicts σ_6. The eigenfunctions are normalized such that $\langle\sigma_i\sigma_i\rangle_\Omega=1$.

The first two eigenfunctions possess the most energy in the lower right corner. Thus, the largest velocity fluctuations take place in that area of the cavity. The structures in the first eigenfunctions are relatively large indicating that large eddies have much energy. The second pair of eigenfunctions has a substantial amount of energy in the lower left corner too. These structures are also rather large. The spatial structures in the lower right corner are smaller than those of the first pair of eigenfunctions. The main difference between the third pair, σ_5^n and σ_6^n, and the second pair seems to be that the eddies in the lower right corner rotate in opposite directions; the eddies in the lower left corner rotate in the same direction.

The next five, $\sigma_7^n,\ldots,\sigma_{11}^n$, and σ_{17}^n, are shown in Fig. 9. Here, the pairing is not so obvious. σ_9^n and σ_{10}^n are the first eigenfunctions with spatial structures in the upper left corner of the cavity. They are approximately a quarter out of phase. The fact that the first eight eigenfunctions do not possess spatial structures in the upper left corner shows that these structures have relatively little (fluctuating) energy.

The seventeenth eigenfunction (see Fig. 9, lower right picture) is the first one with a spatial structure in the center of the cavity, just like the mean flow. Hence, the seventeenth eigenfunction is an important representative for eddies in the center of the cavity. The central structure of σ_{17}^n turns in the direction opposite to the rotation of the central eddy in the mean flow. The energy of the 17th POD mode a_{17}^n and the total kinetic energy are strongly correlated. That is, on average, a decrease of a_{17}^n corresponds to an increase of the total energy (and *vice versa*). σ_{24}^n and σ_{39}^n are the next eigenfunctions with spatial structures in the core of the cavity (not shown). These structures are considerably smaller than the core structure of σ_{17}^n. Even smaller structures in the core of the cavity can be observed in σ_{60}^n, σ_{70}^n, and σ_{80}^n (also not shown).

The (approximate) POD modes form a (nearly) optimal basis for reconstructing a signal. To see how fast a projection on this basis converges, we have randomly selected a veloc-

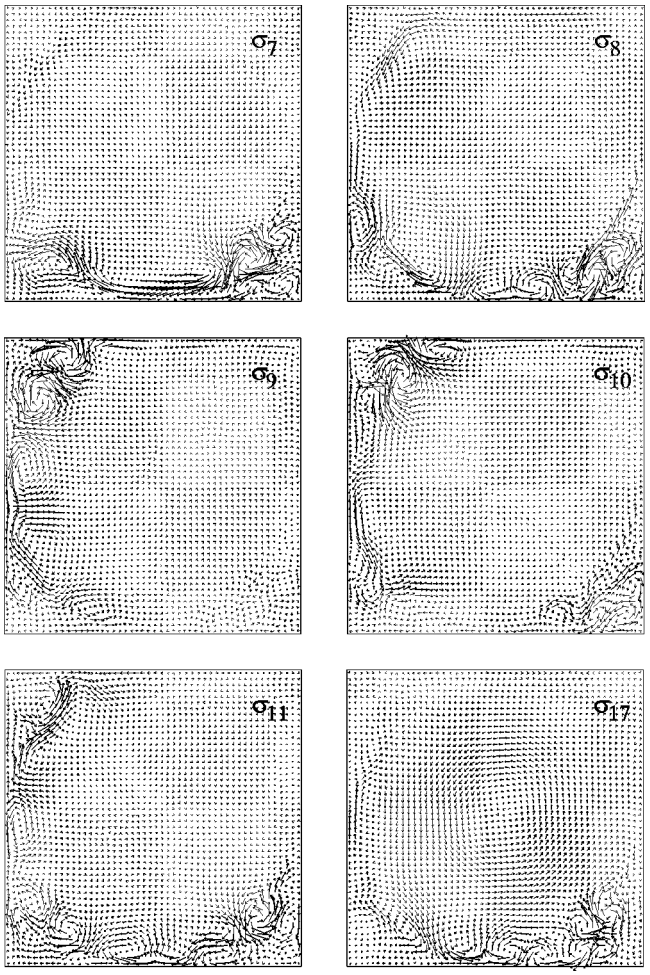

FIG. 9. Vector plots of $\sigma_7, \ldots, \sigma_{11}$ and σ_{17}. The numbering goes in reading order. The lower right picture shows σ_{17}. The seventeenth eigenfunction is the first with a spatial structure in the centre of the cavity.

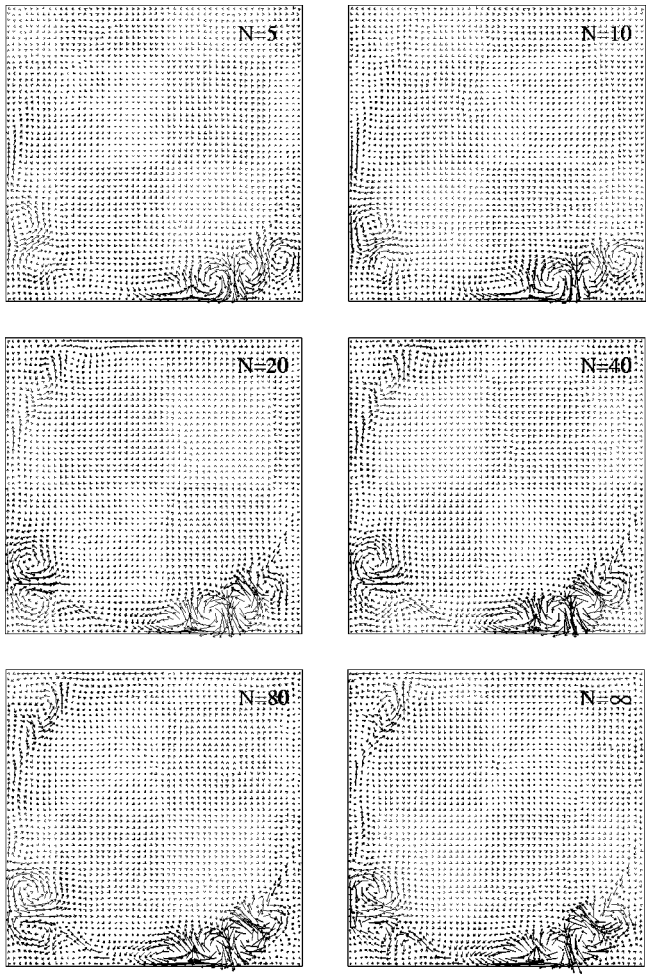

FIG. 10. Projections of a randomly selected fluctuating flow field on the space spanned by the first N σ_i's. The lower right picture shows the sample ($N=\infty$). The other pictures are vector plots of the projections on the first 5, 10, 20, 40, 80 σ_i's, respectively (in reading order).

ity field (not a snapshot) from the DNS. The lower right picture in Fig. 10 shows our sample. The upper left picture in Fig. 10 depicts its projection on $\{\sigma_1^n, \ldots, \sigma_5^n\}$. The most pronouncing difference between the two pictures occurs in the upper left corner of the cavity, where the projection shows no structures, whereas the full field possesses structures. But, what else could the projection on $\{\sigma_1^n, \ldots, \sigma_5^n\}$ be; σ_9^n and σ_{10}^n are the first eigenfunctions with spatial structures in the upper left corner. Yet, also the projection on $\{\sigma_1^n, \ldots, \sigma_{10}^n\}$ (Fig. 10, upper right picture) shows no clear structures in the upper-left corner. For that, the sample has to be projected onto the first twenty σ_i^n's; see Fig. 10. All the large-scale structures are reasonably represented in this projection. When the basis of the projection is increased from 20 to 40 or 80, the adjustments are small and concentrated on the small scales. The coefficients of the projection are depicted in Fig. 11.

IV. LOW-DIMENSIONAL MODELS

The Galerkin projection of the Navier–Stokes equations on the spatial structure σ_i reads as

$$\left\langle \sigma_i \frac{\partial u}{\partial t} \right\rangle_\Omega = -\langle \sigma_i \nabla \cdot (uu) \rangle_\Omega - \frac{1}{Re} \langle \nabla \sigma_i \nabla u \rangle_\Omega . \qquad (4.1)$$

Here we have made use of properties that the divergence of the spatial structures is zero and that they vanish at the

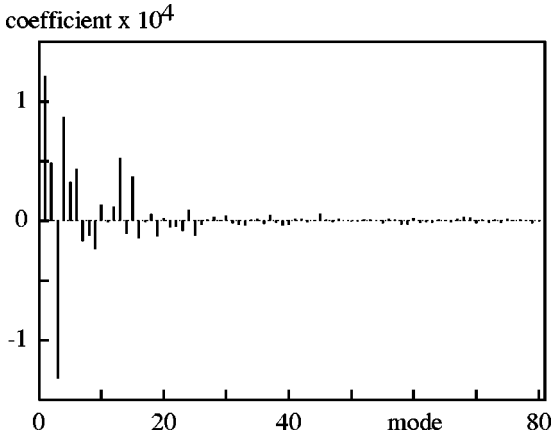

FIG. 11. Coefficients in the expansion of the arbitrary fluctuating velocity field that is shown in Fig. 10.

boundaries. For the discrete POD these two properties are obvious, since any σ_i is a linear combination of snapshots, and every snapshot of u' satisfies these properties. For the continuous POD it can be shown that if all fluctuating velocity fields u' having a certain property form a closed linear subspace, then the spatial structures σ_i have the same property, and the converse is also true; see Ref. 11.

Equation (4.1) forms the basis for our dynamical modeling of the flow in a driven cavity. To obtain a low-dimensional, discrete model (4.1) is to be truncated and discretized in space and time (Section IV A). The effect of the truncation can be neglected (as in Section IV B) or modeled by introducing an artificial dissipation (Section IV C). The latter is not needed for the transition analysis that is performed in Section V; it is just needed for long-term integrations in the turbulent regime ($Re=22{,}000$).

A. Truncation and discretization

We decompose the velocity field $u(x,t)$ into the mean velocity $\langle u\rangle_T$ and the fluctuating velocity $u'(x,t)$, and truncate the projection of u' on the spatial structures σ_i:

$$u(x,t)\approx\langle u\rangle_T+\sum_{i=1}^{N}\alpha_i(t)\sigma_i(x). \tag{4.2}$$

Substituting this approximation into (4.1) shows that the evolution of the temporal coefficients $\alpha_i(t)$ is given by

$$\frac{d\alpha_i}{dt}=-A_{ijk}\alpha_j\alpha_k-B_{ij}\alpha_j-C_i, \tag{4.3}$$

where A_{ijk}, B_{ij}, and C_i depend on the mean flow $\langle u\rangle_T$, the spatial structures $\sigma_i(x)$, and gradients thereof:

$$A_{ijk}=\langle\sigma_i\nabla\cdot(\sigma_j\sigma_k)\rangle_\Omega,$$

$$B_{ij}=\frac{1}{Re}\langle\nabla\sigma_i\nabla\sigma_j\rangle_\Omega+\langle\sigma_i\nabla\cdot(\sigma_j\langle u\rangle_T)\rangle_\Omega+\langle\sigma_i\nabla\cdot(\langle u\rangle_T\sigma_k)\rangle_\Omega,$$

$$C_i=\langle\sigma_i\nabla\cdot(\langle u\rangle_T\langle u\rangle_T)\rangle_\Omega+\frac{1}{Re}\langle\nabla\sigma_i\nabla\langle u\rangle_T\rangle_\Omega.$$

It may be emphasized that a coefficient α_i is not equal to a_i, due to the truncation of the series in the right-hand side of (4.2); $\alpha_i=a_i$ only holds if $N=\infty$, or at least large enough to capture all dynamically significant scales of motion.

In Section V, we will integrate Eq. (4.3) for a range of Reynolds numbers. We will do this by simply altering the Reynolds number Re in the expressions for B_{ij} and C_i. The mean velocity $\langle u\rangle_T$ and the POD-modes σ_i are not changed. The mean velocity $\langle u\rangle_T$ is directly taken from the DNS. Thus, it is also not altered to compensate for the truncation of the system. It may be noted that in a number of papers (see, e.g., Refs. 6 and 9), the mean velocity profile is approximated in terms of the POD-modes before the Galerkin projection is performed. Both Aubry *et al.*[6] and Glauser *et al.*[9] have approximated the mean velocity (in a turbulent boundary layer and in a jet mixing layer, respectively) in terms of Reynolds stresses, so that coherent structures of the truncated system get feedback from the mean flow as the fluctuation varies.

The coefficients A_{ijk}, B_{ij}, and C_i are discretized on the grid of the DNS. The spatial derivatives in these coefficients are discretized exactly like the corresponding derivatives in the DNS. That is, by central, finite-differences on a staggered grid. The integrations over the flow domain Ω are approximated using the trapezoidal rule for numerical integration. For the temporal integration of the thus obtained semi-discrete dynamical system we have tested three numerical methods: the classical fourth-order Runge–Kutta method, Crank–Nicolsons method with a Newton linearization for the non-linear terms, and a fifth-order DOPRI method with a variable step size (details of the DOPRI method can be found in Ref. 32, for example). With all these methods the semi-discrete dynamical system can be integrated accurately with a time step that is (much) larger than the one used for the DNS. From the three methods mentioned above, the DOPRI method performs the best in relation to the costs. Therefore, we have applied the fifth-order DOPRI method.

B. Short-term dynamics

We can close the system given by Eq. (4.3) by simply neglecting all contributions related to spatial structures σ_i with an index i larger than N, i.e., by taking $i,j,k=1,...,N$ in Eq. (4.3). This yields a direct, fully spectral, simulation method for the flow in the driven cavity. Fully spectral methods are rarely used; usually quasi-spectral methods are preferred. In quasi-spectral methods the velocity and its gradient are transformed from spectral space to physical space. After that, the non-linear terms are evaluated in physical space and the result is transformed back to spectral space. This approach is not suited in combination with POD, since a transformation from the physical space to the space spanned by the spatial structures is tremendously expensive to compute. This holds also for the inverse transformation. Therefore we apply a fully spectral method, where the spectral space is spanned by the σ_i's with $i=1,...,N$.

The convergence of the solution of the 20-, 40-, and 80-dimensional dynamical systems (4.3) to the solution of the Navier–Stokes equations is shown in Fig. 12 ($Re=22{,}000$). For this comparison, all time-integrations were started from the same initial condition. That is, after the POD-modes have been computed, we have taken an arbitrary velocity field from the DNS. The projection of this field on the first 20 modes forms the initial condition from which the time-integration of the Navier–Stokes equations restarted, and the time-integration of the 20-, 40-, and 80-dimensional system is started. In Fig. 13 the coefficient of σ_1 is shown during one large-eddy turnover-time.

Figures 12 and 13 demonstrate the potential of the low-dimensional dynamical system (4.3) to approximate the Navier–Stokes equations for relatively short times.

In the next section we consider a closure model to take the energy transfer from and to the neglected, low-energetic, modes into account. It may be remarked that, for the initial condition considered here, the results for short time integra-

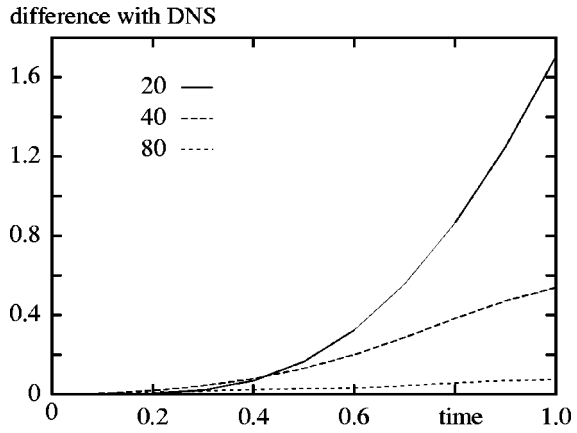

FIG. 12. The difference between the numerical solution of the 20-, 40-, and 80-dimensional model and the solution of the Navier–Stokes equations. This figure shows the time-integral of the absolute difference of the projection of the numerical solution of the Navier–Stokes equations, and that of the dynamical models, on σ_1 versus time.

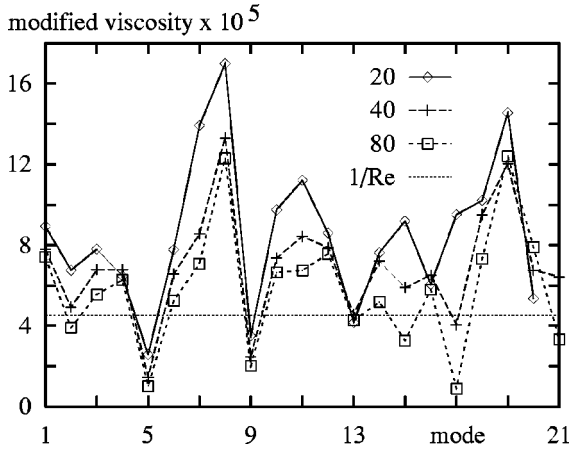

FIG. 14. The modified coefficient $1/R\tilde{e}_i$ as a function of the index i for the 20-, the 40-, and the 80-dimensional model. The reference level $1/Re$ is denoted by the dashed line.

tions do not become significantly better or worse using this closure model. That is, for short times, the result of the low-dimensional model with closure as well as that without diverge exponentially from the Navier–Stokes solution. The time-integral of the absolute difference with the Navier–Stokes solution is in both cases proportional to $\exp(Ct)$, where the constant C depends strongly on the number of modes N, but (practically) not on the closure.

C. Closure model for long-term integrations at *Re*=22,000

For $N=20$, 40, and 80 our direct spectral simulation method does not predict the long-term physics of the flow at $Re=22{,}000$ correctly. That is, after a transient phase, the result of the integration of the dynamical system (4.3) with $i,j,k=1,...,N$ converges to a statistical equilibrium around a state with a much too high energy content. So, we need a (dissipative) closure model to mimic the behavior of the flow in a driven cavity at $Re=22{,}000$ for long times.

Here, we consider a closure model that is based on the average energy exchange between the spatial structures. To

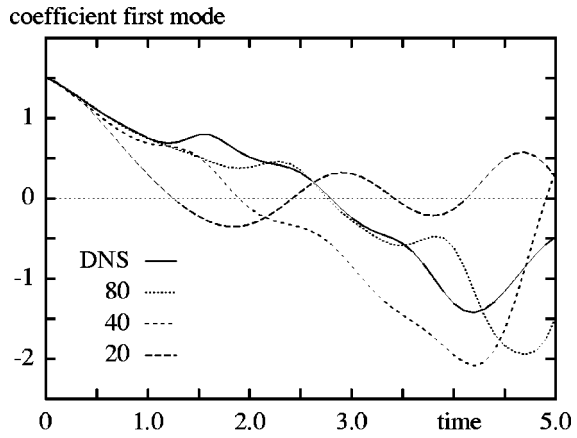

FIG. 13. The projection of the solution on the first eigenfunction σ_1 during one large-eddy turnover-time.

start, the series in the right-hand side of (4.2) is not truncated ($N=\infty$). The coefficients α_i are then equal to a_i. The rate of change of energy in the direction of σ_i is given by $(\alpha_i^2(t))'$. On average the energy a_i^2 has to be conserved: $\langle 2\alpha_i\alpha_i'\rangle_T=0$. Hence,

$$\sum_{j,k} A_{ijk}\langle\alpha_i\alpha_j\alpha_k\rangle_T+B_{ii}\lambda_i=0. \tag{4.4}$$

Note that the average of α_i is zero, and that the α_i's satisfy $\langle\alpha_i\alpha_j\rangle_T=\delta_{ij}\lambda_i$. These properties hold since $\alpha_i=a_i$. Equation (4.4) does not hold if we truncate the system (4.3). To account for the unresolved modes we add a linear damping term $-D_ia_i$ to the right-hand side of (4.3), and take $i,j,k=1,...,N$ (with N small). The value of D_i is determined from the requirement that the energy of the resulting modified finite-dimensional system is conserved:

$$\sum_{j,k=1}^{N} A_{ijk}\langle\alpha_i^m\alpha_j^m\alpha_k^m\rangle_m+(B_{ii}+D_i)\lambda_i=0, \tag{4.5}$$

where the triple product is approximated by averaging over the snapshots used to compute the POD.

We have implemented the artificial damping term $-D_i\alpha_i$ by modifying the coefficient $1/Re$ for the diagonal elements of B_{ij} in order to have a point of reference for the magnitude of the damping that is introduced by the closure model. The modified coefficient is denoted by $1/R\tilde{e}_i$:

$$\frac{1}{R\tilde{e}_i}=\frac{1}{Re}+\frac{D_i}{\langle\nabla\sigma_i\nabla\sigma_i\rangle_\Omega}. \tag{4.6}$$

According to Eq. (4.5) D_i depends on the number of retained modes N, and so does $1/R\tilde{e}_i$. Figure 14 displays the first twenty $1/R\tilde{e}_i$ for $N=20$, 40, and 80. The time-average of the energy dissipated by mode i is given by $\lambda_i\langle\nabla\sigma_i\nabla\sigma_i\rangle_\Omega/Re$ On average, the ratio of the energy transfered from mode i to unresolved modes and the energy that is dissipated by mode i is equal to $Re/R\tilde{e}_i-1$. This ratio is at most 2.7 ($N=20$), 1.8 ($N=40$), and 1.7 ($N=80$). For all three values of N the maximum value is obtained for $i=8$. Figure 14 shows that,

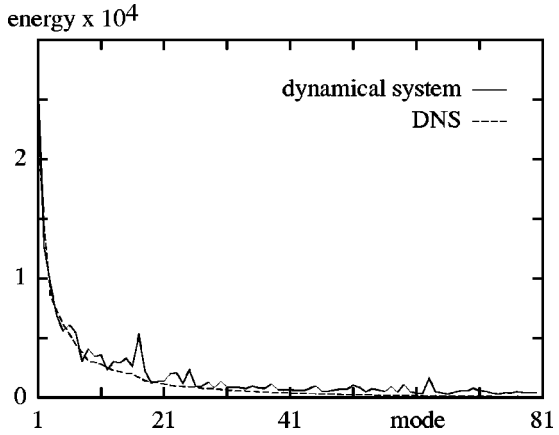

FIG. 15. The spectrum of the 80-dimensional dynamical system with the adjusted closure model. Note the peak in the energy of the 17-th eigenfunction (see the text).

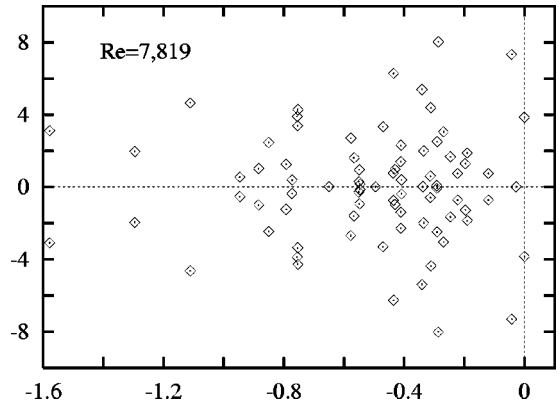

FIG. 16. Eigenvalues of the Jacobian of the linearized 80-dimensional system at $Re=7{,}819$. A pair of complex conjugate eigenvalues crosses the imaginary axis.

on average, the coefficients tend to $1/Re$ when more modes are retained. Yet, the modes for which the corresponding coefficient $1/R\tilde{e}_i$ is smaller than $1/Re$ for $N=80$ seem not to be converged. It may be emphasized that these modes are not damped, but blown up, by the closure model. The coefficient $1/R\tilde{e}_{46}$ becomes even negative for $N=80$ (not shown in Fig. 14).

Runs with the closure model outlined above showed that the results of long-term integrations are better than those without the closure model, but are still not in fair agreement with the results of the DNS at $Re=22{,}000$. Therefore we adjust the closure model: instead of $1/R\tilde{e}_i$ we take

$$\frac{1}{R\bar{e}_i}=\max\left\{\frac{1}{Re},\frac{1}{R\tilde{e}_i}\right\}, \tag{4.7}$$

so that the closure model is dissipative for all modes. Figure 15 shows the spectrum as obtained from a long time integration with the closure given by (4.7). Compared to the spectrum of the DNS (the dotted line in Fig. 15) the tail of the spectrum of the 80-dimensional model is somewhat lifted up, but the general picture is correct. The 80-dimensional model is reasonably able to reproduce the spectrum of the DNS, albeit that the closure given by (4.7) is still open for improvement: the modes for which the damping coefficient is limited to $1/Re$ ($i=17$, for example) peak too high in the spectrum. To improve the closure, the energy budgets need to be considered, as in Ref. 33.

V. TRANSITION BEHAVIOR OF AN 80-DIMENSIONAL MODEL

In this section, we perform a transition analysis of the low-dimensional dynamical system (4.3) for $N=80$. For this N, 95% of the fluctuating energy is captured ($Re=22{,}000$). The system is closed as described in Section IV B, that is, the effect of the non-resolved modes is simply neglected. We will refer to the thus obtained dynamical system as the 80-dimensional model. As far as possible, the stability of steady and periodic solutions of the 80-dimensional model will be compared to the results obtained with DNS (in Section II C).

In Section V A, a linear stability analysis of the steady flow in the cavity is performed with the help of the 80-dimensional model. The stability of periodic solutions of the 80-dimensional model is considered in Section V B.

A. Stability of steady states

The solution of the 80-dimensional model converges rapidly to a steady state for $Re=5{,}000$. To determine the stability of this steady state we have linearized the 80-dimensional dynamical system around this state and computed the eigenvalues of the Jacobian: all have negative real parts. Thus, small disturbances of the steady state are damped for $Re=5{,}000$.

The eigenvalues of the Jacobian move towards the imaginary axis when the Reynolds number is increased. To determine the point where one or more eigenvalues cross the imaginary axis we have computed the Jacobian at two different Reynolds numbers and have extrapolated the smallest negative real part of the eigenvalues to zero (assuming that the dependence on the Reynolds number is linear). By iterating this procedure we have found that at $Re=7{,}819$ a pair of complex conjugate eigenvalues crosses the imaginary axis (see Fig. 16). So, the first (Hopf) bifurcation of the 80-dimensional model takes place at (approximately) $Re=7{,}819$. The eigenvector that corresponds to the unstable pair of complex conjugate eigenvalues is shown in Fig. 17. Obviously, some kind of vortex-street is developing along the edge of the primary eddy in the core of the cavity. The velocities are largest in the lower-right corner of the cavity, where the shear-stress is also maximal. This indicates a shear-layer instability along the edge of the primary eddy.

Poliashenko and Aidun[26] have also computed the first bifurcation point of the flow in a square lid-driven cavity. They did not compute eigenvalues of the Jacobian directly, but used a alternative technique which they have applied to the incompressible Navier–Stokes equations. They found that the first transition from a steady state occurs at $Re=7{,}763$ and estimated the (discretization) error in this bifurcation point at $\pm 2\%$. The difference between their critical Reynolds number and that of the 80-dimensional dynamical system is approximately 0.7%. The streamlines of their dis-

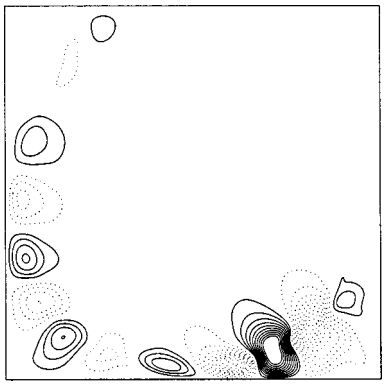

FIG. 17. Streaklines of the unstable eigenvector of the 80-dimensional model at $Re=7{,}819$. The solid lines indicate a clockwise turning direction and the dotted lines indicate a counter-clockwise turning direction.

turbance look like the unstable eigenvector depicted Fig. 17, and they also concluded that the first bifurcation is due to the centrifugal instability of the primary eddy. In addition, they noted that at the threshold of Hopf bifurcation, there are four other complex-conjugate eigenvalues with relatively small real parts and one small real eigenvalue. This can be observed in Fig. 16, too.

To re-examine the first transition of the 80-dimensional model we have performed fourth-order accurate direct numerical simulations of the flow in a lid-driven cavity at $Re=8{,}000$, $Re=8{,}100$, $Re=8{,}200$, and $Re=8{,}400$. From the results of these four simulations the critical value of the Reynolds number is estimated at $Re=7{,}972$; see Section II C. This number lies about 2% above the critical Reynolds number of the 80-dimensional model.

Thus, the 80-dimensional model predicts the Reynolds number at which the first transition of the flow in a driven cavity occurs accurately and the growing disturbances look correct compared to Ref. 26. Yet, the frequency of the periodic solution that arises after the first bifurcation is not predicted well by the 80-dimensional model: it yields a frequency of about 3.85, whereas Poliashenko and Aidun[26] and our DNS give $2.86\pm1\%$ and 2.85, respectively.

After the first bifurcation non-linear terms come into play and continuing the linear stability analysis of the steady-state solution seems to be meaningless at first sight. Yet, as we will see in the next section, this is not the case. Therefore, we continue the linear stability analysis of the steady-state solution.

At $Re=8{,}214$ a second pair of eigenvalues crosses the imaginary axis, as shown in Fig. 18 (the top picture). The frequency belonging to this instability is higher than that belonging to the first instability. The eigenvector associated with this second instability is shown in the right (top) plot of Fig. 18. Like the first eigenvector, also the second eigenvector displays a vortex street along the primary eddy in the core of the cavity. The size of the eddies is smaller than before. Further increasing the Reynolds number leads to a third, fourth, and fifth pair of eigenvalues crossing the imaginary axis (see Fig. 18). Here, it may be emphasized that the second pair returns to the complex left half-plane before the fourth pair crosses the imaginary axis. All eigenvectors display a vortex street. The size of the eddies that form the vortex street is smaller for the higher frequencies than for the lower frequencies. The largest velocity fluctuations appear in the lower right corner for all but the fifth instability. The fifth eigenvector has the largest fluctuations in the lower left side of the cavity.

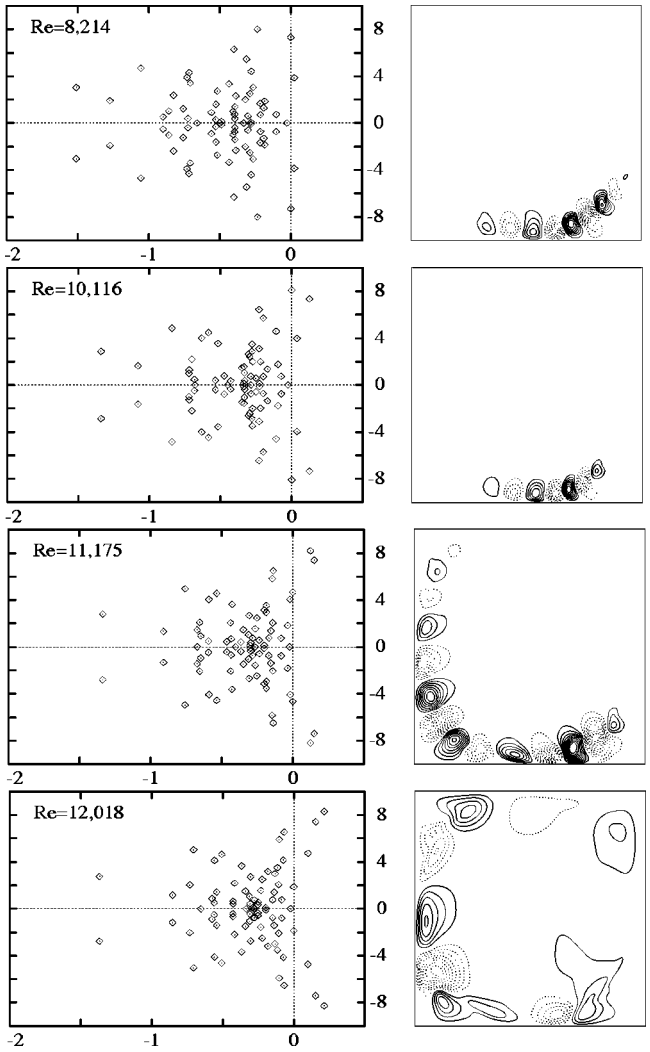

FIG. 18. Subsequent instabilities of the unstable steady state. Eigenvalues of the Jacobian (left) and streaklines (right) of the eigenvector belonging to the eigenvalue at the imaginary axis. The solid lines indicate a clockwise turning direction and the dotted lines indicate a counter-clockwise turning direction.

B. Stability of periodic solutions

As far as we know, the stability of periodic driven cavity flows has remained unexplored. The stability of a periodic solution is determined by its Floquet multipliers. We denote the cross section of a periodic orbit in the state space by Σ. A periodic solution intersects Σ in one point p. The Poincaré map P maps points q of Σ in some neighborhood $U\subset\Sigma$ of p by following the solution through q until it first crosses Σ. A periodic orbit is stable if all points $q\in U$ converge to p under the iteration of P. This holds, if all the eigenvalues of the linearization of the map P at p, the Floquet multipliers, lie in the unit disc in the complex plane.

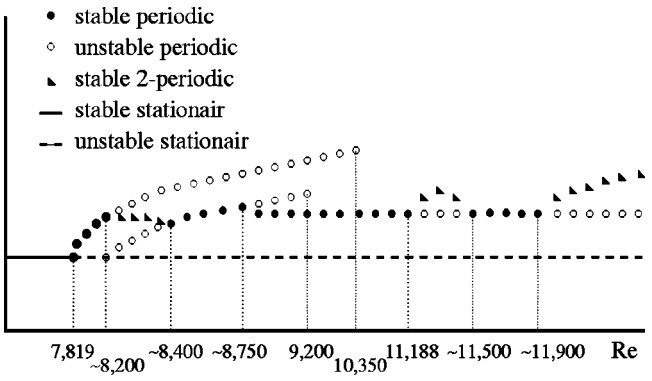

FIG. 19. Qualitative bifurcation diagram of the 80-dimensional dynamical system. Not all the bifurcations from the steady-state solution are shown for simplicity. Note that the horizontal axis is not linear.

Periodic solutions have been computed using a shooting method (see, for instance, Ref. 34). The method starts with a solution sufficiently close to a periodic orbit. This initial solution is determined by either a time-integration (for stable solutions) or is taken equal to a solution at a slightly different Reynolds number that has been determined previously. Also a reasonable estimate of the period is needed. From this starting point the 80-dimensional dynamical system is integrated over one period. If the difference between the solution after one period and the initial solution is not zero, a Newton iteration is started and is continued until a periodic state is reached.

Thus, we have computed the periodic solution of the 80-dimensional system at $Re=8{,}000$. This solution is stable: all its Floquet multipliers lie within the unit disc. Both our linear stability analysis of the 80-dimensional model and the analysis of the Navier–Stokes equations in Ref. 26 showed that there are four complex conjugate pairs of eigenvalues with small real parts and one small negative eigenvalue at the point of the first instability (Figure 16). This indicates that the transition of the flow is complicated.

The transition behavior of the 80-dimensional model is summarized in Fig. 19. The characteristic points of this graph are discussed in the sequel.

At $Re=8{,}200$ a pair of complex conjugate Floquet multipliers leaves the unit disc, as is shown in Fig. 20(a). (Note that a Floquet multiplier $+1$ is always present since the dynamical model does not explicitly depend on the time t.) Figure 21(a) shows the eigenvector that corresponds to the unstable mode. The two frequencies of the solution at $Re=8{,}200$ are 3.85 and 7.30, i.e., the fast part oscillates approximately 1.9 times around the slow part. The ratio between the imaginary parts of the first two pairs of unstable eigenvalues of the Jacobian of the steady-state solution (see Fig. 18) is also approximately 1.9. Hence, the Floquet analysis and the linear analysis give similar results here.

The unstable periodic solution stays unstable for higher Reynolds numbers. A second pair of Floquet multipliers leaves the unit disc at approximately $Re=10{,}350$. Somewhat later, at $Re=10{,}700$, a Floquet multiplier leaves the unit disc at -1 indicating a period-doubling. Unfortunately, we can not follow this branch of solutions with our method, since these (unstable) solutions have more than one period.

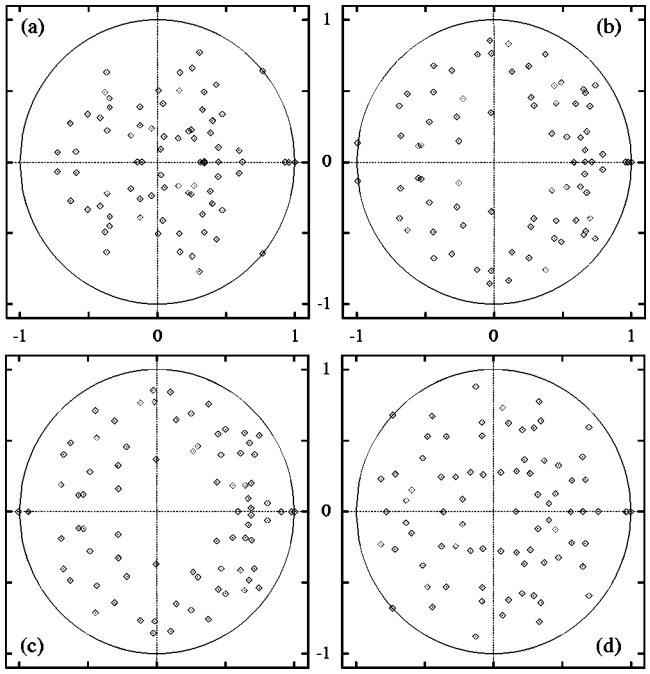

FIG. 20. Floquet multipliers of periodic solutions of the 80-dimensional system at $Re=8{,}200$ (a), $Re=8{,}400$ (b), $Re=8{,}750$ (c), and $Re=11{,}118$ (d). The Floquet multipliers move in and out the unit disc. Figure (a) shows a pair of complex conjugate multipliers that leaves the unit disc. In Fig. (b), a pair of complex conjugate multipliers enters the unit disc; in (c) a real multiplier leaves the unit disc at -1. In Fig. (d), a pair of complex conjugate multipliers leaves the unit disc.

The stable 2-periodic solution that appears after the bifurcation at $Re=8{,}200$ becomes 1-periodic again at approximately $Re=8{,}400$. Its frequency (7.30) corresponds to that of the second pair of unstable eigenvalues of the Jacobian (see Fig. 18). In Fig. 20(b) the Floquet multipliers which enter the unit disc are shown. They correspond to an unstable periodic solution that becomes stable. The solution with a frequency of 7.30 stays stable till approximately $Re=8{,}750$.

The behavior of the 80-dimensional system in the range between $Re=8{,}200$ and $Re=8{,}750$ is not confirmed by the results of the DNS presented in Section II C. It is possible that this behavior is an artifact of the model (i.e., that the model is destabilized by the truncation), or that we overlook

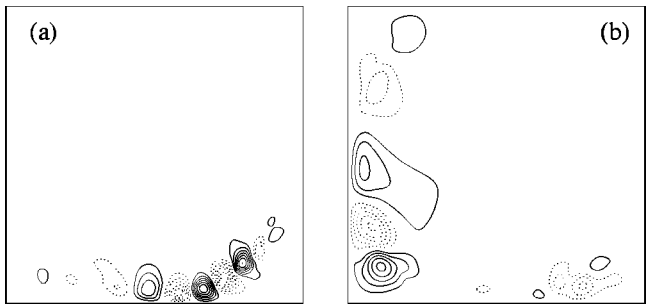

FIG. 21. Streaklines of the eigenvectors corresponding to the unstable Floquet multipliers at $Re=8{,}200$ (a) and $Re=11{,}118$ (b). The unstable Floquet multipliers are shown in Fig. 20.

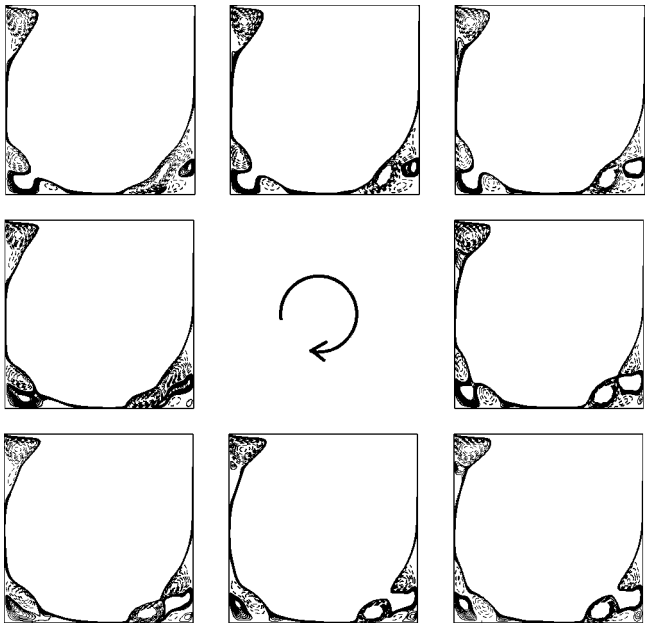

FIG. 22. Streaklines of one period of the periodic solution of the 80-dimensional system at $Re=11{,}800$. Solid lines indicate a clockwise rotation, and dashed lines indicate counter-clockwise rotation (compare Fig. 5).

frequencies with a small amplitude in the DNS-data (like many others did, when they stated that the flow is stationary up to and including $Re=10{,}000$). Here, a stability analysis of the Navier–Stokes equations should give a decisive answer.

At $Re=8{,}750$ a Floquet multiplier leaves the unit disc at -1, indicating a period-doubling [see Fig. 20(c)]. We have followed the unstable periodic solution with the frequency 7.30 until $Re=9{,}200$. This solution is rather unstable: it has a large Floquet multiplier. The stable periodic solution that arises after the period-doubling stays stable for Reynolds numbers up to $Re=11{,}188$. Hence, it exists for a relatively large range of Reynolds numbers. Moreover, its frequency is almost equal to that of the stable solution after the first Hopf bifurcation.

At $Re=11{,}188$ a pair of complex conjugate Floquet multipliers leaves the unit disc as is shown in Fig. 20(d). The two frequencies of the stable solution are 3.77 and 2.33. Their ratio $3.77/2.33=1.62$ is comparable to that of the two frequencies of the 2-periodic solution obtained with the DNS at $Re=11{,}000$ (see Section II C): $2.7/1.7=1.6$. Thus, the angle at which the Floquet multipliers leave the unit disc is predicted well by the 80-dimensional model; the absolute values of the frequencies are not predicted accurately (at $Re\approx 11{,}000$). Moreover, the Reynolds number at which the flow becomes quasi-periodic is too high: the DNS yields a two-periodic solution at $Re=10{,}000$; the 80-dimensional model bifurcates at $Re=11{,}188$.

For somewhat higher Reynolds numbers both the DNS and the 80-dimensional model have again periodic solutions. At $Re=11{,}500$ a pair of complex conjugate eigenvalues reenters the unit disc. The frequency of the solutions of the 80-dimensional model for Reynolds numbers in the range $Re=11{,}500-11{,}900$ (i.e., 3.74) is almost the same as the frequency (3.7) of a periodic solution of the DNS at $Re=12{,}000$. The (stable) periodic solution of the 80-dimensional model at $Re=11{,}800$ is shown in Fig. 22. It displays qualitatively the same behavior as the result of the DNS at $Re=12{,}000$ that is shown in Fig. 5.

VI. CONCLUSIONS

In this paper, a proper orthogonal decomposition of a 2D flow in a lid-driven cavity at $Re=22{,}000$ is computed (from DNS data) to educe the coherent structures in this flow and to construct a 80-dimensional dynamical model for it. The following conclusions can be drawn from this study. By utilizing their space–time symmetry, POD-modes can be computed efficiently. The first 80 spatial POD modes capture (on average) 95% of the fluctuating kinetic energy. They, indeed, educe the coherent structures in the flow. A projection of the Navier–Stokes equation on them gives a 80-dimensional dynamical system. We have evaluated this 80-dimensional model by comparing the results of its transition analysis with data from direct numerical simulation for Reynolds numbers in the range $Re=8{,}000-12{,}000$. The agreement with the available DNS-data is good, albeit that the stability analysis of periodic solutions of the 80-dimensional model also reveals some complicated transitions that we could not yet confirm by means of DNS.

ACKNOWLEDGMENTS

The Stichting Nationale Computerfaciliteiten (National Computing Facilities Foundation, NCF) with financial support from the Nederlandse Organisatie voor Wetenschappelijk Onderzoek (Netherlands Organization for Scientific Research, NWO) is gratefully acknowledged for the use of supercomputer facilities.

[1] J. L. Lumley, ''The structure of inhomogeneous turbulent flows,'' in *Atmospheric Turbulence and Radio Wave Propagation*, edited by A. M. Yaglom and V. I. Tararsky (Nauka, Moscow, 1967), pp. 166–178.
[2] M. Loeve, *Probability Theory* (Van Nostrand, New York, 1955).
[3] N. Aubry, ''On the hidden beauty of the proper orthogonal decomposition,'' Theor. Comput. Fluid Dyn. **2**, 339 (1991).
[4] W. Cazemier, ''Proper orthogonal decomposition and low-dimensional models for turbulent flows, Ph.D. thesis, University of Groningen, The Netherlands, 1997.
[5] R. Témam, *Infinite Dimensional Dynamical Systems in Mechanics and Physics* (Springer-Verlag, New York, 1989).
[6] N. Aubry, P. Holmes, J. L. Lumley, and E. Stone, ''The dynamics of coherent structures in the wall region of a turbulent boundary layer,'' J. Fluid Mech. **192**, 115 (1988).
[7] A. E. Deane, I. G. Kevrekidis, G. E. Karniadakis, and S. A. Orsag, ''Low-dimensional models for complex geometry flows: Application to grooved channels and circular cylinder,'' Phys. Fluids A **3**, 2337 (1991).
[8] A. E. Deane and C. Mavriplis, ''Low-dimensional description of the dynamics in separated flow past thick airfoils,'' AIAA J. **6**, 1222 (1994).
[9] M. N. Glauser, S. J. Leib, and W. K. George, ''Coherent structures in the axisymmetric turbulent jet mixing layer,'' in *Turbulent Shear Flows 5*, edited by F. Durst *et al.* (Springer-Verlag, New York, 1987).
[10] D. Rempfer and H. F. Fasel, ''Evolution of three-dimensional coherent structures in a flate-plate boundary layer,'' J. Fluid Mech. **260**, 351 (1994).
[11] G. Berkooz, P. Holmes, and J. L. Lumley, ''The proper orthogonal decomposition in the analysis of turbulent flows,'' Annu. Rev. Fluid Mech. **25**, 539 (1993).
[12] P. Holmes, J. L. Lumley, and G. Berkooz, *Turbulence, Coherent Structures, Dynamical Systems and Symmetry* (Cambridge Monographs on Mechanics (Cambridge University Press, Cambridge, 1996).

[13]L. Sirovich, ''Turbulence and the dynamics of coherent structures. Part III: Dynamics and scaling,'' Q. Appl. Math. **45**, 583 (1987).
[14]Z.-C. Liu, R. J. Adrian, and T. J. Hanratty, ''Reynolds number simularity of orthogonal decomposition of the outer layer of turbulent wall flow,'' Phys. Fluids **6**, 2815 (1994).
[15]B. R. Noack and H. Eckelmann, ''A low-dimensional Galerkin method for the three-dimensional flow around a circular cylinder,'' Phys. Fluids **6**, 124 (1994).
[16]A. E. P. Veldman and K. Rinzema, ''Playing with nonuniform grids,'' J. Eng. Math. **26**, 119 (1992).
[17]J, Meijerink and H. van der Vorst, ''An iterative solution method for linear systems of which the coefficient matrix is a symmetric M-matrix,'' Math. Comput. **31**, 148 (1977).
[18]I. Gustafson, ''A class of first-order factorization methods,'' BIT **18**, 142 (1978).
[19]R. W. C. P. Verstappen and A. E. P. Veldman, ''Direct numerical simulation of turbulence at lower costs,'' J. Eng. Math. **32**, 143 (1997).
[20]R. W. C. P. Verstappen and A. E. P. Veldman, ''Spectro-consistent discretization of Navier–Stokes: a challenge to RANS and LES,'' to appear in J. Eng. Math.
[21]R. W. C. P. Verstappen, J. G. Wissink, and A. E. P. Veldman, ''Direct numerical simulation of driven cavity flows,'' Appl. Sci. Res. **51**, 377 (1993).
[22]P. Grassberger and I. Procaccia, ''Characterization of strange attractors,'' Phys. Rev. Lett. **50**, 346 (1983).
[23]P. Grassberger and I. Procaccia, ''Estimation of the Kolmogorov entropy from a chaoctic signal,'' Phys. Rev. A **28**, 2591 (1983).
[24]J. N. Sørensen and O. Daube, ''Direct simulation of flow structures initiated by a rotating cover in a cylindrical vessel,'' in *Advances in Turbulence 2*, edited by H.-H. Fernholz and H. E. Fieldler (Springer-Verlag, Berlin, 1989), pp. 383–390.
[25]U. Ghia, K. N. Ghia, and C. T. Shin, ''High-Re solutions for incompressible flow using the Navier–Stokes equations and a multigrid method,'' J. Comput. Phys. **48**, 387 (1982).
[26]M. Poliashenko and C. K. Aidun, ''A direct method for computation of simple bifurcations,'' J. Comput. Phys. **121**, 246 (1995).
[27]J. E. Marsden and M. McCracken, *The Hopf Bifurcation and its Application* (Springer-Verlag, Berlin, 1976).
[28]K. Liffman, ''Comments on a collocation spectral solver for the Helmholtz equation,'' J. Comput. Phys. **128**, 254 (1996).
[29]J. N. Sørensen, M. O. L. Hansen, and E. A. Christensen, ''Numerical investigation of symmetry breakdown in a cylindrical lid driven cavity,'' in *Computational Fluid Dynamics '96*, edited by J.-A. Désidéri *et al.* (Wiley, Chichester, 1996), pp. 439–444.
[30]L. Sirovich, ''Turbulence and the dynamics of coherent structures. Part I: Coherent structures,'' Q. Appl. Math. **45**, 561 (1987).
[31]S. G. Mikhlin, *Integral Equations, and their Applications to Certain Problems in Mechanics, Mathematical Physics and Technology* (Pergamon, Oxford, 1957).
[32]E. Hairer, S. P. Nørsett, and G. Wanner, *Solving Non-Linear Differential Equations I* (Springer-Verlag, Berlin, 1991).
[33]G. Berkooz, P. Holmes, and J. L. Lumley, ''On the relation between low-dimensional models and the dynamics of coherent structures in the turbulent wall layer,'' Theor. Comput. Fluid Dyn. **4**, 255 (1993).
[34]M. Kubiček and M. Marek, *Computational Methods in Bifurcation Theory and Dissipation Structures* (Springer-Verlag, Berlin, 1983).